Thermohaline layering in dynamically and diffusively stable shear flows

Timour Radko†

Department of Oceanography, Naval Postgraduate School, Monterey, CA 93943, USA

In this study we examine two-component shear flows that are stable with respect to
Kelvin–Helmholtz and to double-diffusive instabilities individually. Our focus is on
diffusively stratified ocean regions, where relatively warm and salty water masses are
located below cool fresh ones. It is shown that such systems may be destabilized by
the interplay between shear and thermohaline effects, caused by unequal molecular
diffusivities of density components. Linear stability analysis suggests that parallel
two-component flows can be unstable for Richardson numbers exceeding the critical
value for non-dissipative systems ($Ri = 1/4$) by up to four orders of magnitude. Direct
numerical simulations indicate that these instabilities transform the initially linear
density stratification into a series of well-defined horizontal layers. It is hypothesized
that the combined thermohaline–shear instabilities could be ultimately responsible for
the widespread occurrence of thermohaline staircases in diffusively stable regions of
the World Ocean.

Key words: convection, double diffusive convection

---

1. Introduction

This study contributes to the discussion of the origin of thermohaline staircases in
high-latitude regions of the World Ocean. The term thermohaline staircase describes a
series of mixed layers separated by thin high-gradient interfaces, commonly observed
in vertical profiles of temperature and salinity. Staircases in the Arctic and Southern
Oceans are typically diffusive, with warm salty water masses located below those that
are relatively cold and fresh. Diffusive staircases often exhibit remarkable spatial and
temporal coherence. For instance, layers of the Beaufort Gyre staircase in the Arctic
Ocean maintain their identity across hundreds of kilometres laterally and over several
years of observation (e.g. Timmermans *et al.* 2008).

Despite the profound importance of staircases for high-latitude ocean dynamics
(Turner 2010; Flanagan, Lefler & Radko 2013), the physical cause of diffusive
layering has not been fully explained (Kelley *et al.* 2003; Radko 2013). It is generally
accepted that staircases are ultimately produced and maintained by double-diffusive
processes. A major challenge in the development of a complete theory of high-latitude

† Email address for correspondence: tradko@nps.edu

staircases is to explain the initiation of layering and diffusive convection from smooth original distributions of temperature and salinity. The parameter range for diffusive instability in the ocean is extremely narrow (e.g. Walin 1964; Veronis 1965):

$$1 < R_\rho < \frac{Pr + 1}{Pr + \tau},$$ (1.1)

where R_ρ is the diffusive density ratio, i.e. the ratio of vertical gradients of temperature and salinity, normalized by the expansion/contraction coefficients, $\tau = k_S/k_T$ is the diffusivity ratio and $Pr = \nu/k_T$ is the Prandtl number. Here, k_T and k_S are the molecular diffusivities of temperature and salinity, and ν is the molecular viscosity. For oceanic parameters ($\tau \sim 0.01$, $Pr \sim 10$), condition (1.1) reduces to $1 < R_\rho < 1.1$, and this interval lies outside the density ratio range typical for oceanic diffusive staircases ($1.5 < R_\rho < 10$). The typical internal wave energy and associated vertical shears in the Arctic at the staircase depth range (150–300 m) are also weak (e.g. Levine, Paulson & Morison 1985; Halle & Pinkel 2003; Cole *et al.* 2014). As a result, the representative values of the Richardson number (Ri), the measure of flow susceptibility to dynamic instability, are high ($Ri \sim 10$), substantially exceeding the threshold value of $Ri = 1/4$ required for dynamic instability. Hence, the background stratification is generally stable with respect to both primary diffusive and dynamic instabilities.

To rationalize the propensity for layering in stably stratified waters, several hypotheses have been proposed. The applied flux mechanism (Turner & Stommel 1964; Kelley *et al.* 2003) assumes the presence of an external source of buoyancy (e.g. heating from below or, equivalently, cooling from above) which is sufficiently strong to produce top-heavy stratification in the immediate vicinity of the forcing region. The ensuing localized convection creates a well-mixed region and concurrently transfers buoyancy vertically, leading to the formation of an adjacent convecting layer. The process then repeats several times, eventually producing a multilayer staircase. The proposed scenario is actually realized in laboratory experiments, in which a staircase is created by heating the bottom of a tank filled with doubly stratified fluid (Turner & Stommel 1964; Fernando 1987). However, in the ocean interior, outside of geothermal heating zones and the subsurface mixed layer, buoyancy forcing is too weak and lacks sufficient variation with depth to consistently generate large-scale convective overturns.

Stern (2003) suggested that the transition from the smooth-gradient regime to the staircase configuration in a stable halocline could be initiated by lateral molecularly-driven interleaving (Holyer 1983), which, in turn, is contingent on the presence of horizontal temperature and salinity (T–S) gradients. What casts some doubt on the generality of this mechanism is that staircases exist throughout the Arctic diffusive zone and no correlation has been reported between the incidences of layering and the strength of lateral isopycnal gradients. Another possible pathway to thermohaline layering stems from the tendency of diffusive systems to be destabilized by fundamentally nonlinear processes (Veronis 1965). While Veronis' effect undoubtedly plays a role in the transition to fully developed diffusive convection, it requires large-amplitude perturbations of unspecified origin. Thus, a complete and satisfying explanation of layering calls for some additional dynamical considerations. Furthermore, simulations in our study indicate that staircases can form spontaneously even in the absence of lateral property gradients, large-amplitude initial disturbances or external heating, which suggests that none of the aforementioned phenomena are essential for diffusive layering.

This paper argues for adding a new candidate to the list. We point out that even when a two-component flow is stable with respect to dynamic and diffusive instabilities individually, it may become unstable due to the interplay between shear and thermohaline effects. This conclusion is supported by a Floquet-based stability analysis for a sinusoidal velocity profile in a fluid linearly stratified in the diffusive sense. The growth rates and stability conditions are shown to be highly sensitive to the diffusivity ratio of the density components. Direct numerical simulations (DNS) indicate that the combined thermohaline–shear instabilities can indeed trigger the transition of uniformly stratified systems to well-defined staircases. In this regard, it is interesting to mention that strong large-scale shears can have adverse effects on the coherence and persistence of thermohaline staircases (e.g. Bebieva & Timmermans 2016). Yet, somewhat counterintuitively, the vertical shear could also be essential for their generation.

Of course, destabilization driven by buoyancy diffusion is a known phenomenon which can occur even in one-component flows (e.g. Balmforth & Young 2002; Radko & Stern 2011; Thorpe, Smyth & Li 2013). However, in non-double-diffusive models, this effect is modest. It affects only a relatively narrow parameter range $(Ri \lesssim 1)$ and does not lead to the formation of persistent staircases. The growth rates in this extended range are much lower than those typical of Kelvin–Helmholtz instability. In contrast, the double-diffusive case is characterized by the appearance of a fundamentally new and dramatic phenomenon which bears little resemblance to either dynamic or diffusive oscillatory instabilities. Both shear and the unequal diffusivities of density components are essential, and the stability boundary can reach surprisingly high values – for instance, it could be as high as $Ri \sim 10^3$ for $R_\rho = 2$. Such unrestrictive conditions are easily met in the Arctic Ocean, which lends credence to our proposition that diffusive layering could be initiated by thermohaline–shear instability.

It is also interesting to note that the origin of salt-finger staircases, in which warm and salty water is located above cold and fresh, has proven to be a simpler and less controversial subject than diffusive layering. Fingering staircases are found in tropical and mid-latitude ocean regions that are already susceptible to primary (salt-finger) instabilities. These microscale perturbations produce vertical fluxes of heat and salt that are modulated by large-scale T–S gradients. The interplay between finger-driven fluxes and vertical gradients leads to the spontaneous generation of secondary double-diffusive structures – thermohaline staircases, collective instability waves and intrusions. Plausible theories of finger-driven layering based on the instability of flux-gradient laws have already been developed and numerically validated (Merryfield 2000; Radko 2003; Stellmach *et al.* 2011; Radko 2014). The diffusive problem considered here is very different. The static basic state in this case is linearly stable in the relevant parameter regime, and therefore even the origin of primary perturbations is uncertain.

The paper is organized as follows. The model set-up is described in § 2. Section 3 presents numerical evidence for spontaneous layering in shear flows that are dynamically and diffusively stable, suggesting the existence of a new type of instability. This proposition is supported by linear stability analysis based on the Floquet theory (§ 4). In § 5, we discuss the energetics – and offer physical interpretation – of the thermohaline–shear instability. The results are summarized and the conclusions are drawn in § 6.

2. Formulation

The temperature and salinity fields (T^*_{tot}, S^*_{tot}) are separated into linear vertical background profiles (T^*_{bg}, S^*_{bg}) and a departure (T^*, S^*) from them:

$$\left.\begin{array}{l} T^*_{tot} = T^*_{bg} + T^* = A_T z^* + A_{T0} + T^*, \\ S^*_{tot} = S^*_{bg} + S^* = A_S z^* + A_{S0} + S^*, \end{array}\right\} \tag{2.1}$$

where $(A_T, A_{T0}, A_S, A_{S0})$ are constants. The asterisks hereafter denote dimensional quantities and the subscripts '*tot*' represent the total field variables. Our focus is on the diffusive case, in which both temperature and salinity decrease upward: $\partial T^*_{bg}/\partial z^* = A_T < 0$ and $\partial S^*_{bg}/\partial z^* = A_S < 0$. In the present version of the theory, we ignore planetary rotation, compressibility and the nonlinearity of the equation of state, which reduces the governing Boussinesq equations of motion to

$$\left.\begin{array}{l} \dfrac{\partial T^*}{\partial t^*} + \boldsymbol{v}^*_{tot} \cdot \nabla T^* + w^*_{tot} \dfrac{\partial T^*_{bg}}{\partial z^*} = k_T \nabla^2 T^*, \\[2mm] \dfrac{\partial S^*}{\partial t^*} + \boldsymbol{v}^*_{tot} \cdot \nabla S^* + w^*_{tot} \dfrac{\partial S^*_{bg}}{\partial z^*} = k_S \nabla^2 S^*, \\[2mm] \dfrac{\partial \boldsymbol{v}^*_{tot}}{\partial t^*} + \boldsymbol{v}^*_{tot} \cdot \nabla \boldsymbol{v}^*_{tot} = -\dfrac{1}{\rho_0} \nabla p^*_{tot} + g(\alpha T^* - \beta S^*)\boldsymbol{k} + \nu \nabla^2 \boldsymbol{v}^*_{tot}, \\[2mm] \nabla \cdot \boldsymbol{v}^*_{tot} = 0, \end{array}\right\} \tag{2.2}$$

where $\boldsymbol{v}^*_{tot} = (u^*_{tot}, v^*_{tot}, w^*_{tot})$ is the velocity, p^*_{tot} is the dynamic pressure, g is gravity and (α, β) are the thermal expansion and haline contraction coefficients.

Consider the basic state (denoted by overbars) representing unidirectional shear flow with a sinusoidal velocity profile:

$$\bar{u}^*(z^*) = U_0 \sin\left(\frac{2\pi z^*}{H}\right), \quad \bar{v}^* = \bar{w}^* = \bar{T}^* = \bar{S}^* = 0. \tag{2.3a,b}$$

It is assumed that the shear (2.3) is maintained against viscous dissipation by the externally imposed pressure gradient force

$$\frac{\partial \bar{p}^*}{\partial x^*} = -\frac{4\pi^2 \nu \rho_0 U_0}{H^2} \sin\left(\frac{2\pi z^*}{H}\right). \tag{2.4}$$

For convenience, the governing equations are non-dimensionalized using H as the unit of length, U_0 as the unit of velocity and H/U_0 as the unit of time. The non-dimensionalization is implemented as follows:

$$\left.\begin{array}{l} (u^*, v^*, w^*) \to U_0(u, v, w), \quad p^* \to \rho_0 U_0^2 p, \\[2mm] \alpha T^* \to \alpha \left|\dfrac{\partial T^*_{bg}}{\partial z^*}\right| HT, \quad \beta S^* \to \alpha \left|\dfrac{\partial T^*_{bg}}{\partial z^*}\right| HS, \\[2mm] (x^*, y^*, z^*) \to H(x, y, z), \quad t^* \to \dfrac{H}{U_0} t, \end{array}\right\} \tag{2.5}$$

which transforms the governing equations to

$$\left.\begin{array}{l} \dfrac{\partial T}{\partial t} + \boldsymbol{v}_{tot} \cdot \boldsymbol{\nabla} T - w_{tot} = \dfrac{1}{Pe} \nabla^2 T, \\[3mm] \dfrac{\partial S}{\partial t} + \boldsymbol{v}_{tot} \cdot \boldsymbol{\nabla} S - R_\rho w_{tot} = \dfrac{\tau}{Pe} \nabla^2 S, \\[3mm] \dfrac{\partial \boldsymbol{v}_{tot}}{\partial t} + \boldsymbol{v}_{tot} \cdot \boldsymbol{\nabla} \boldsymbol{v}_{tot} = -\boldsymbol{\nabla} p_{tot} + \dfrac{4\pi^2 Ri}{R_\rho - 1}(T - S)\boldsymbol{k} + \dfrac{Pr}{Pe} \nabla^2 \boldsymbol{v}_{tot}, \\[3mm] \boldsymbol{\nabla} \cdot \boldsymbol{v}_{tot} = 0, \end{array}\right\} \quad (2.6)$$

where

$$R_\rho = \frac{\beta \dfrac{\partial S_{bg}^*}{\partial z^*}}{\alpha \dfrac{\partial T_{bg}^*}{\partial z^*}} \quad (2.7)$$

is the background density ratio,

$$Ri = \frac{N_b^2 H^2}{4\pi^2 U_0^2} = \alpha \left| \frac{\partial T_{bg}^*}{\partial z^*} \right| \frac{gH^2}{4\pi^2 U_0^2}(R_\rho - 1) \quad (2.8)$$

is the Richardson number, N_b is the buoyancy frequency, $Pe = (U_0 H)/k_T$ is the Peclet number, $\tau = k_S/k_T$ is the diffusivity ratio and $Pr = \nu/k_T$ is the Prandtl number. It should be noted that the Richardson number is based on the maximal shear $(2\pi U_0/H)$. While this convention leads to a rather cumbersome coefficient of the buoyancy term in the vertical momentum equation, it represents the most physical definition of the Richardson number. The Peclet number can also be expressed in terms of Ri and N_b as follows:

$$Pe = \sqrt{Ri} \frac{N_b H^2}{2\pi k_T}. \quad (2.9)$$

Representative values of the Richardson number and the buoyancy frequency in the diffusive regions of the World Ocean are $Ri \sim 1 - 10$, $N_b \sim 10^{-3} s^{-1}$. The relevant vertical scale of the basic shear that could trigger thermohaline–shear instabilities is highly uncertain. If we assume that $H \sim 1m$, then (2.9) implies $Pe \sim 10^3$, which provides very rough guidance for the exploration of the parameter space. The basic state (2.3), (2.4) reduces in non-dimensional units to

$$\bar{u}(z) = \sin(2\pi z), \quad \bar{p}_x = -(2\pi)^2 \frac{Pr}{Pe} \sin(2\pi z), \quad \bar{v} = \bar{w} = \bar{T} = \bar{S} = 0. \quad (2.10a\text{-}c)$$

The non-dimensional perturbation velocity and pressure are defined accordingly as

$$\boldsymbol{v} = (u_{tot} - \bar{u}, v_{tot}, w_{tot}), \quad p = p_{tot} - \bar{p}. \quad (2.11a,b)$$

3. Direct numerical simulations

Preliminary insights into thermohaline–shear destabilization were first generated from numerical solutions. The governing equations (2.6) were integrated in time using the dealiased pseudospectral method (e.g. Stern, Radko & Simeonov 2001; Stellmach *et al.* 2011) with periodic boundary conditions applied to the perturbation

fields in each spatial direction. Both two- and three-dimensional DNS were performed. Double-diffusive DNS are computationally expensive, particularly for thermohaline layering experiments. In this case, it becomes necessary to resolve a wide range of dynamically significant scales – from the anticipated step height, which greatly exceeds the scale of heat dissipation, to the salinity dissipation scale, which is smaller than the heat scale by a factor of $\sqrt{\tau}$. In this study we consider oceanographically relevant parameters $(Pr, \tau) = (10, 0.01)$, and such a small diffusivity ratio restricts the integration periods accessible by three-dimensional DNS. Two-dimensional DNS are certainly less demanding computationally and can be used to simulate relatively weak instabilities evolving on longer time scales. Furthermore, as will be shown here, they adequately capture key features of the nonlinear evolution of thermohaline–shear instabilities – staircase formation and subsequent layer-merging events.

Figure 1 presents a typical 3D simulation. The chosen parameters $(Ri, R_\rho, Pe) = (0.5, 2, 10^4)$ define a system that is individually stable with respect to dynamic and to diffusive instabilities. This calculation was initiated by the basic state (2.10) perturbed by small-amplitude random initial (T, S) distributions. The computational domain $(L_x, L_y, L_z) = (2, 1, 1)$, which corresponds to a dimensional size of 6 m × 3 m × 3 m, was resolved by a numerical mesh with $768 \times 384 \times 384$ grid points. The evolution of this system is illustrated by a sequence of temperature perturbation snapshots (figure 1*a–f*). It should be noted that the perturbation initially (figure 1*a*) attains its largest values in the low-shear part of the flow ($z \approx 3/4$) – one of the many features distinguishing this phenomenon from Kelvin–Helmholtz instability. This pattern gradually amplifies in time, leading to a substantial nonlinear modification of the vertical stratification and shear. As a result, the Richardson number is reduced below the critical value of $Ri_{cr} = 1/4$ in selected locations and becomes susceptible to Kelvin–Helmholtz instabilities. These secondary instabilities, clearly visible in figure 1(*b*), tend to be localized to high-shear ($z \approx 0, 1/2, 1$) regions. The ensuing mixing produces a series of well-defined horizontally uniform layers (figure 1*c*). While the layers formed initially are relatively thin, they merge sequentially, until there is only one well-defined layer left by $t = 20\,902$ (figure 1*f*).

The layering dynamics is revealed more clearly by the plots (figure 2) of the total horizontally averaged density profiles, which include the contribution from linear background stratification:

$$\rho_{mean} = \langle S - T \rangle + (1 - R_\rho)z, \tag{3.1}$$

where $\langle \cdots \rangle$ denotes averaging in (x, y). These profiles demonstrate the formation of relatively homogeneous layers separated by high-gradient interfaces – structures that are suggestive of the observed thermohaline staircases. The transition from uniformly stratified to layered systems is slow, with a growth rate of $\lambda \sim 1.5 \times 10^{-3}$, which corresponds to a dimensional time scale of several days.

During the early stages of the experiment (figure 1*a,b*), the perturbation is relatively uniform in the *y*-direction, which suggests that the most rapidly growing instability mode is quasi-two-dimensional and therefore the linear phase can be adequately represented by the 2D model. This proposition was readily confirmed by reproducing the foregoing simulation in two dimensions (x, z) and observing similar evolutionary patterns. For instance, figure 3 presents an analogous two-dimensional experiment for $Ri = 1$ (all other parameters were kept the same). The increase in the Richardson number results in a much lower growth rate ($\lambda \sim 2 \times 10^{-4}$), which places this case beyond the current capabilities of 3D DNS. Nevertheless, this system evolves in
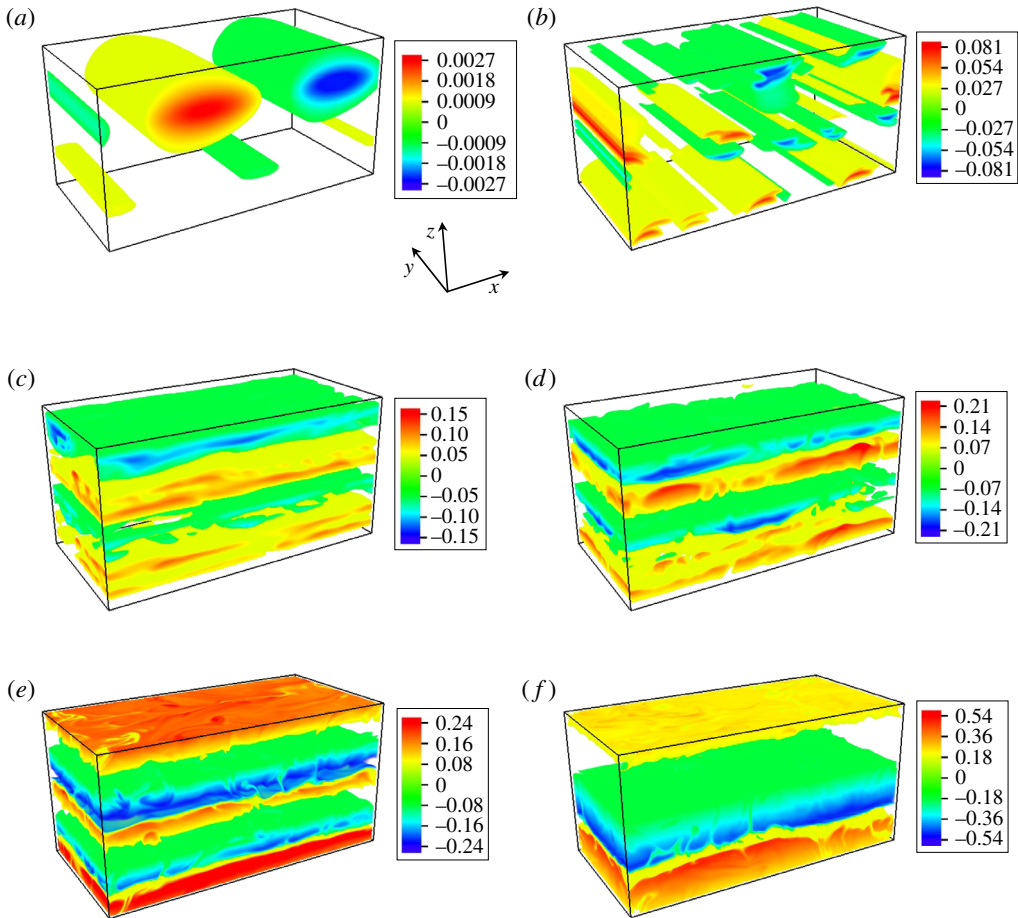
FIGURE 1. (Colour online) Three-dimensional DNS of layering in the dynamically and diffusively stable regime $(R_\rho, Ri, Pe, \tau) = (2, 0.5, 10^4, 0.01)$. The instantaneous temperature perturbations are shown in $(a–f)$ at $t = 4012, 5007, 6010, 7054, 15\,014$ and $20\,902$ respectively.

a very similar manner – the compact perturbation localized in the low-shear zone gradually amplifies (figure 3a–c) and eventually transforms the uniform stratification into a well-defined staircase. As previously (cf. figure 2), the layers that are formed first are not steady but undergo a series of merging events, until there is only one step left within the limits of the computational domain. The tendency for layers to merge is a generic property of thermohaline staircases, which is realized in both diffusive and fingering configurations, in two and in three dimensions (e.g. Radko *et al.* 2014*a,b*).

The relatively slow evolution of the perturbations in figures 1–3 is consistent with our interpretation that these instabilities are being driven by the molecular diffusion of density components. Since the foregoing simulations are only weakly dissipative ($Pe = 10^4$), it is not surprising that the corresponding non-dimensional growth rates are also very low ($\lambda \sim 10^{-3}$–10^{-4}). The reduction in the Peclet number, however, dramatically increases both the growth rates and the parameter range
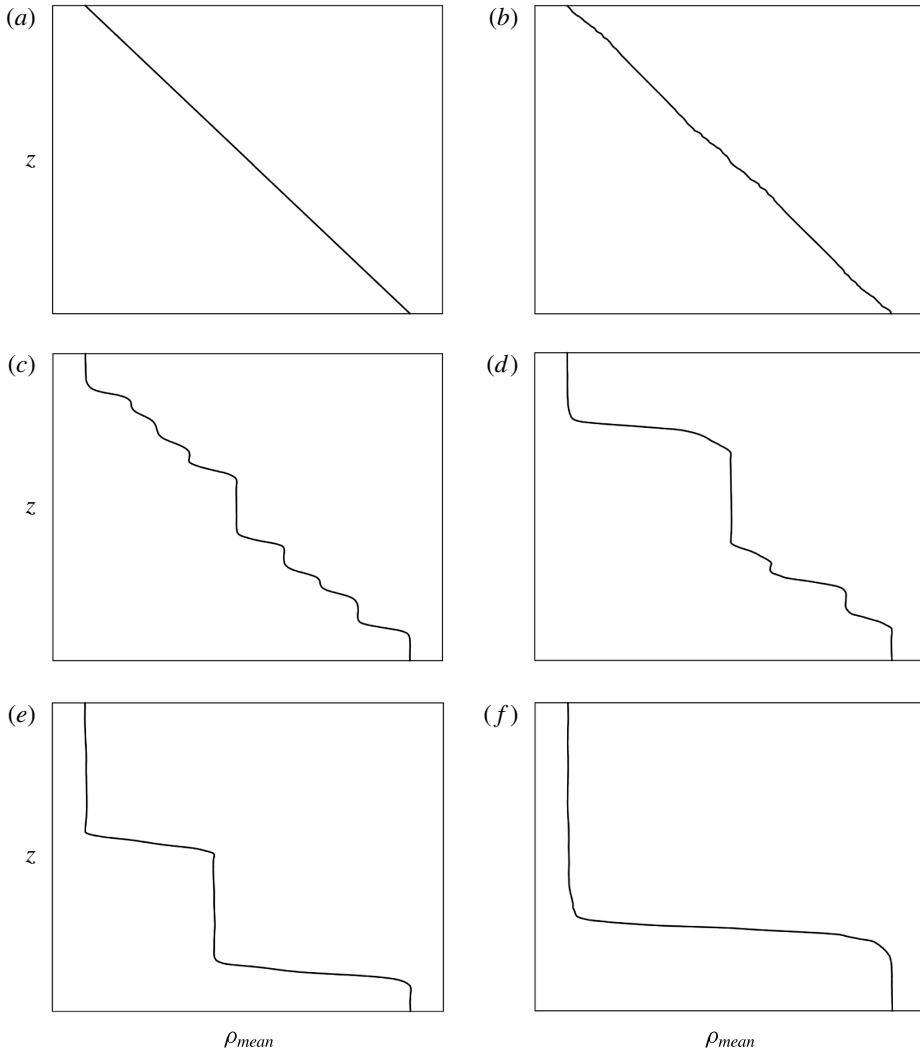
FIGURE 2. The horizontally averaged density profiles for the simulation in figure 1. One can note the formation of relatively small homogeneous layers separated by high-gradient interfaces (*c*) and their subsequent merger (*d–f*).

of thermohaline–shear instability. Figure 4, for instance, presents the simulation performed for $(Pe, Ri) = (100, 10)$. The perturbation in this case amplifies much faster ($\lambda \sim 0.02$), and the Richardson number is a factor of 40 greater than the critical value of $Ri_{cr} = 1/4$ suggested by classical theory for non-dissipative shear flows (Richardson 1920; Howard 1961; Miles 1961).

Another notable difference between the low-*Pe* (figure 4) and high-*Pe* (figure 3) simulations is the much larger ratio of the vertical/horizontal wavenumbers (m/k) in the unstable modes. This ratio was $m/k \sim 2$ in high-*Pe* experiments, but the most unstable solutions were found for $m/k \sim 50$ in low-*Pe* cases, a finding that is supported and rationalized by the following (§ 4) linear stability analysis. However, there are a number of similarities in the evolution of the low-*Pe* system in figure 4 and high-*Pe*
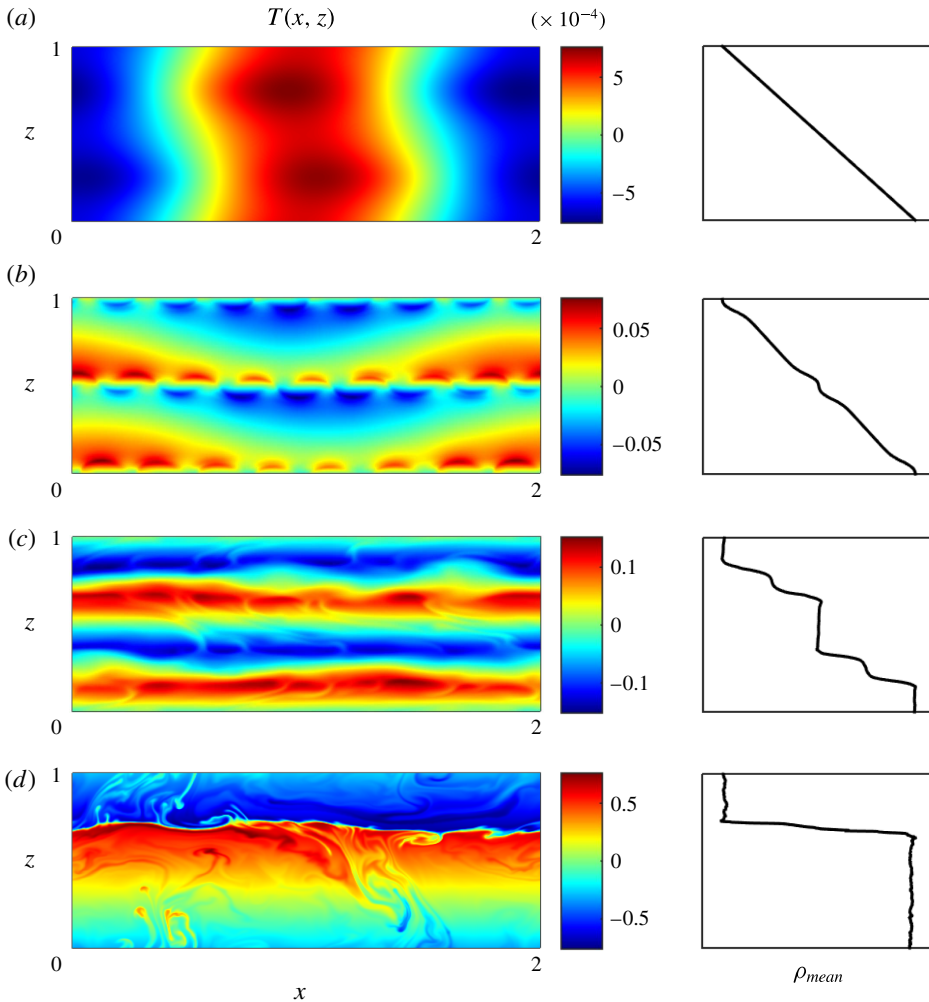
FIGURE 3. (Colour online) Two-dimensional DNS of layering for $(R_\rho, Ri, Pe, \tau) = (2, 1, 10^4, 0.01)$. The instantaneous temperature perturbations are shown in the left panels and the horizontally averaged density profiles are on the right for $t = 30\,575, 49\,020, 52\,118$ and $55\,823$ in (*a–d*) respectively.

systems (e.g. figure 3) as well. The transition starts with the exponential growth of unstable perturbations (figure 4*a,b*). When instabilities amplify to a level sufficient to substantially modify the vertical density and velocity gradients, they produce isolated regions that are susceptible to Kelvin–Helmholtz instability (figure 4*c*). These secondary instabilities manifest themselves in the form of relatively narrow eddies, with $O(1)$ lateral extent, which are clearly visible in the late stages of the experiment (figure 4*c,d*). The ensuing intense mixing generates patches of relatively uniform density separated by interfaces (figure 4*d*). Since the system in figure 4 is much more dissipative than our previous examples, the staircase is not as well defined as in figures 1–3. The interfaces are diffused considerably by molecular dissipation and the mixed layers are not as homogeneous as in high-*Pe* simulations. Nevertheless, we expect that in nature, the initiation of layering by means of thermohaline–shear
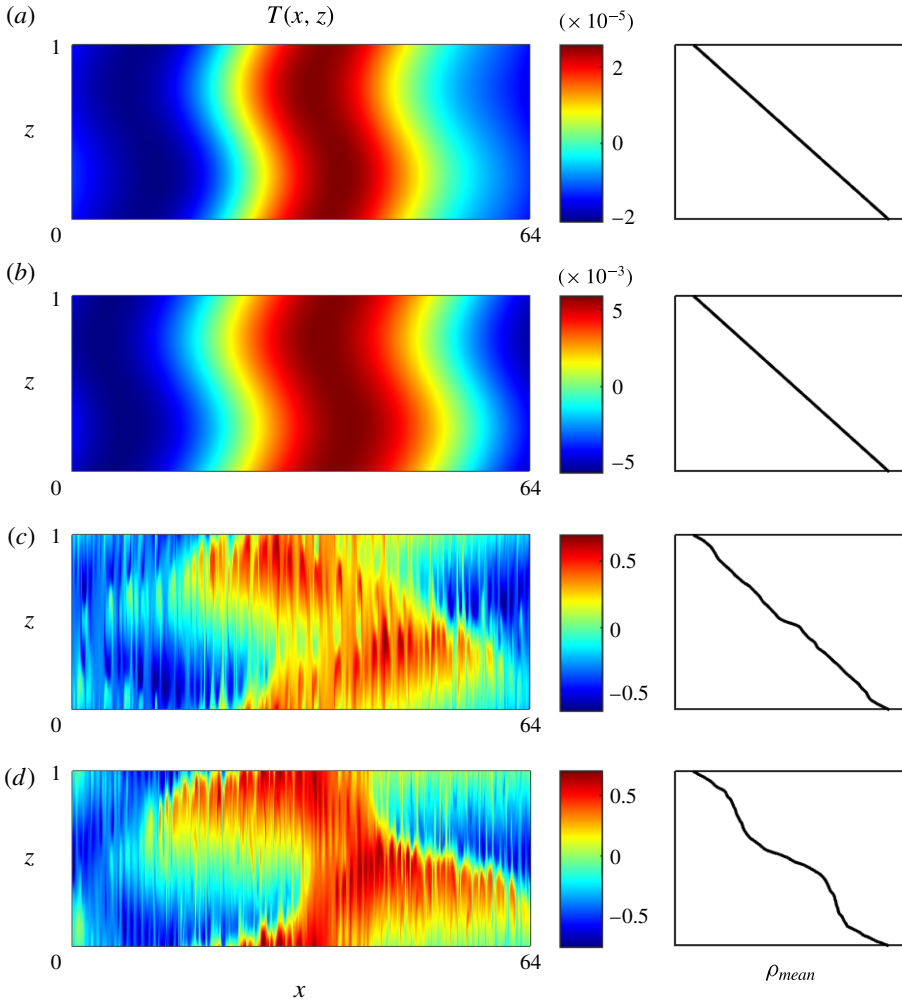
T. Radko

FIGURE 4. (Colour online) Two-dimensional DNS in the low-*Pe* regime: $(R_\rho, Ri, Pe, \tau) = (2, 10, 10^2, 0.01)$. The instantaneous temperature perturbations are shown in the left panels and the horizontally averaged density profiles are on the right for $t = 108, 311, 500$ and 600 in (*a*–*d*) respectively.

instability represents only the first evolutionary stage. Layer-merging events (e.g. Radko *et al.* 2014*a,b*) can systematically increase the step heights in the staircase, concurrently increasing the effective Peclet number, and eventually produce a series of thick well-defined layers.

Numerical support for the layer-merging hypothesis is provided by the simulation in figure 5, which is identical in all respects to the calculation in figure 4, except that the vertical size of the computational domain is now $L_z = 64$. As expected, the dominant vertical scale of instability modes that emerge first matches the wavelength of the basic shear (figure 5*a*). These modes produce a system of horizontal layers. In time, however, layers merge sequentially and their number reduces from $N = 64$ at $t = 1009$ (figure 5*a*) to $N = 3$ at $t = 4040$ (figure 5*d*). The merging pattern is revealed very clearly in the space–time diagram of the horizontally averaged density gradient
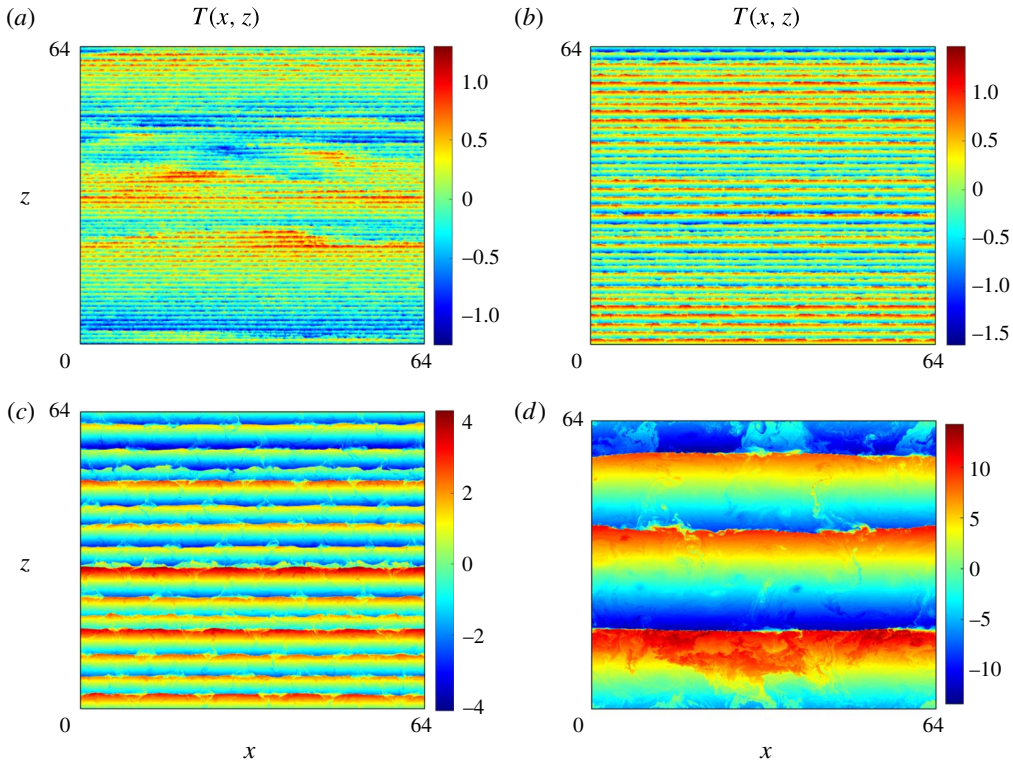
FIGURE 5. (Colour online) Two-dimensional DNS in the low-*Pe* regime: $(R_\rho, Ri, Pe, \tau) = (2, 10, 10^2, 0.01)$. The vertical extent of the computational domain is increased relative to that in figure 4 to $L_z = 64$. The instantaneous temperature perturbations are shown for $t = 1009, 2005, 3500$ and 4040 in (*a*–*d*) respectively.

$-\partial \rho_{mean}/\partial z$ (figure 6*a*). Radko (2007) suggested that layered systems can exhibit two merging patterns: *B* and *H* modes. *B*-mergers represent the strengthening of stronger interfaces at the expense of weaker interfaces, which gradually erode. *H*-mergers occur when interfaces drift vertically and coalesce. Figure 6(*a*) indicates that both *H*- and *B*-mergers are realized, although *H*-mergers are more common. This feature is somewhat unusual since non-sheared double-diffusive systems are generally more susceptible to *B*-mergers (e.g. Radko *et al.* 2014*a*,*b*). Our finding that the average layer thickness greatly increases in time suggests that the effective step height is not directly controlled by the vertical shear scale (*H*). This is an encouraging result. It opens prospects for developing theoretical models of the equilibrium-layer thickness without the explicit knowledge of the relevant wavelength of the basic shear, a quantity that is poorly constrained by observations or models. It should be noted that the non-dimensional layer thickness of $h \sim 20$ realized at the final stages of this experiment (figure 5*d*) can be converted to dimensional values using (2.9), resulting in

$$h^* = h \left(\frac{4\pi^2 k_T^2 RiPe^2}{N_b^2} \right)^{1/4} \sim 10 \text{ m}, \tag{3.2}$$

which is broadly consistent with step sizes of diffusive staircases observed in the Arctic and Southern Oceans (e.g. Kelley *et al.* 2003).

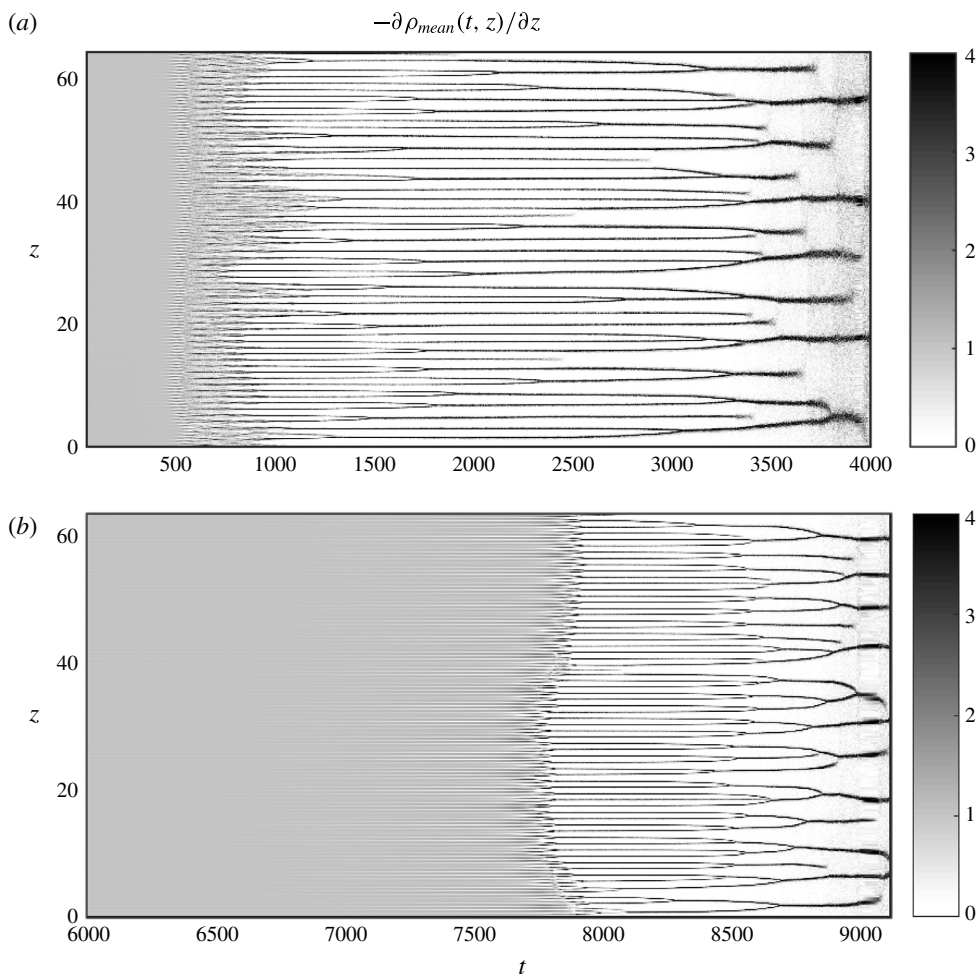(*a*) $-\partial\rho_{mean}(t,z)/\partial z$

(*b*)

t

FIGURE 6. (*a*) Space–time diagram of the mean density gradient for the experiment in figure 5. (*b*) Space–time diagram for the experiment in which $Ri = 100$; other parameters are the same as in (*a*).

Figure 6(*b*) presents an analogous experiment in which the Richardson number is increased to $Ri = 100$. The outcome is qualitatively similar. The spontaneous transition from uniform to stepped stratification starts with the formation of relatively thin layers, the scales of which are set by the periodicity of the background shear. These layers then undergo a series of mergers, which systematically increases the average layer thickness in the staircase. The time scale of the transition is, however, significantly longer for $Ri = 100$ than for $Ri = 10$. The initial layering does not occur until $t = 6000$ – which corresponds to a dimensional time scale of years – whereas in figure 6(*a*) ($Ri = 10$) layers are already visible at $t = 500$.

4. Linear stability analysis

The preliminary experiments (§ 3) revealed that dynamically and double-diffusively stable flows in the ocean can be unstable with respect to mixed thermohaline–shear

instability, and its nonlinear evolution can ultimately produce layered stratification. Therefore, this section offers a more systematic description of thermohaline–shear instability by means of a Floquet-based linear stability analysis.

To examine stability properties of doubly stratified shear flows, the governing equations are first linearized with respect to the basic state (2.10), resulting in

$$
\left.\begin{array}{r}
\dfrac{\partial T}{\partial t} + \sin(2\pi z)\dfrac{\partial T}{\partial x} - w = \dfrac{1}{Pe}\nabla^2 T, \\[2mm]
\dfrac{\partial S}{\partial t} + \sin(2\pi z)\dfrac{\partial S}{\partial x} - R_\rho w = \dfrac{\tau}{Pe}\nabla^2 S, \\[2mm]
\dfrac{\partial u}{\partial t} + \sin(2\pi z)\dfrac{\partial u}{\partial x} + 2\pi w\cos(2\pi z) = -\dfrac{\partial p}{\partial x} + \dfrac{Pr}{Pe}\nabla^2 u, \\[2mm]
\dfrac{\partial v}{\partial t} + \sin(2\pi z)\dfrac{\partial v}{\partial x} = -\dfrac{\partial p}{\partial y} + \dfrac{Pr}{Pe}\nabla^2 v, \\[2mm]
\dfrac{\partial w}{\partial t} + \sin(2\pi z)\dfrac{\partial w}{\partial x} = -\dfrac{\partial p}{\partial z} + \dfrac{4\pi^2 Ri}{R_\rho - 1}(T - S) + \dfrac{Pr}{Pe}\nabla^2 w, \\[2mm]
\nabla\cdot\boldsymbol{v} = 0,
\end{array}\right\}
\tag{4.1}
$$

where the velocity and pressure perturbations are defined in (2.11). The solution is sought in the following form, suggested by the Floquet theory:

$$
\begin{pmatrix} T \\ S \\ u \\ v \\ w \\ p \end{pmatrix} = \exp(\mathrm{i}kx + \mathrm{i}ly + \mathrm{i}m_f z + \lambda t)\sum_{n=-N}^{N} \begin{pmatrix} T_n \\ S_n \\ u_n \\ v_n \\ w_n \\ p_n \end{pmatrix} \exp(2\pi\mathrm{i}nz),
\tag{4.2}
$$

where λ is the growth rate, k and l are the horizontal wavenumbers, and m_f is the Floquet coefficient, which controls the fundamental wavelength in z. When (4.2) is substituted into the linear system (4.1) and the individual Fourier components are collected, the stability problem reduces to the matrix form

$$
\lambda\boldsymbol{\xi} = \boldsymbol{A}\boldsymbol{\xi},
\tag{4.3}
$$

where

$$
\boldsymbol{\xi} = (T_{-N}, S_{-N}, u_{-N}, v_{-N}, w_{-N}, p_{-N}, \ldots, T_N, S_N, u_N, v_N, w_N, p_N),
\tag{4.4}
$$

and $\boldsymbol{A}$ is the $(12N + 2) \times (12N + 2)$ matrix, whose elements are functions of $k, l, m_f, Pe, R_\rho, Ri, N$.

For each set of governing parameters, the eigenvalue with the maximum real part determines the growth rate of the most rapidly amplifying mode. The spatial pattern of the perturbation is then reconstructed from the corresponding eigenvector $\boldsymbol{\xi}$:

$$
\tilde{T} = Re[\exp(\mathrm{i}kx + \mathrm{i}ly + \mathrm{i}m_f z)\sum_{n=-N}^{N} T_n\exp(2\pi\mathrm{i}nz)],
\tag{4.5}
$$

where $\tilde{T}$ represents the temperature distribution in the fastest growing mode. The patterns of S, $\boldsymbol{v}$ and p in the normal modes are reconstructed in a similar manner.

Extensive experimentation with the model indicated that the most rapid growth occurs when the Floquet factor is zero. This means that the fastest growing mode of instability has the same periodicity as that of the shear, and $m_f = 0$ will be used in all subsequent calculations. Likewise, testing the performance of the model for different resolutions revealed that $N = 100$ is sufficient for an accurate representation of the thermohaline–shear instabilities in the considered parameter range, and this value will be employed hereafter.

Figure 7 presents some typical experiments in which Ri and Pe are varied while other parameters are held constant: $(R_\rho, Pr, \tau) = (2, 10, 10^{-2})$. The growth rate $\mathrm{Re}(\lambda)$ is plotted as a function of (k, l) for $(Ri, Pe) = (1, 10^4), (1, 10^2), (10, 10^2)$ in $(a$–$c)$ respectively. In all cases, the system is stable with respect to dynamic and diffusive instabilities individually. Yet, it is apparently destabilized by the interaction between weak shear and two-component stratification (figure 7a–c). The maximal growth rate rapidly increases with decreasing Pe. For instance, the growth rate in the high-Pe regime (figure 7a) is less by two orders of magnitude than in the low-Pe case (figure 7b) for the same Ri. The decrease in Pe also shifts the (non-dimensional) wavelength of the fastest growing mode to much larger values. For the same Pe, a reduction in shear (larger Ri) results in considerably lower growth rates (cf. figure 7b,c). It is important to emphasize that in all cases considered, the largest growth rates were always attained for $l = 0$, which means that the wave fronts of the most rapidly amplifying perturbations are aligned perpendicular to the direction of the basic current. All of these features are consistent with the observed evolution of thermohaline–shear instabilities in DNS (§ 3).

In figure 8, we plot the representative spatial pattern of the most rapidly amplifying mode for $(Ri, Pe) = (1, 10^4)$, which was reconstructed using (4.5). The amplitude of this mode was normalized by the maximal value of the temperature perturbation, and the resulting solution is denoted by $(\hat{T}, \hat{S}, \hat{u}, \hat{w})$. As observed in high-$Pe$ DNS (figures 1, 3), the unstable perturbations in the temperature and salinity fields tend to be localized to the low-shear part of the flow. Because of the symmetry of our system, there are two modes corresponding to the same (largest) growth rate: one is centred at $z = 1/4$ and another, the mirror image of the first, at $z = 3/4$. In figure 9, the same calculation is performed for a low-Pe case: $(Ri, Pe) = (10, 10^2)$. In this regime, the structure of the fastest growing normal mode is substantially different. The temperature perturbation is relatively uniform at all z-levels (figure 9a). Salinity, on the other hand, tends to be localized in the high-shear zones ($z \approx 0, 1/2, 1$). In both low-Pe and high-Pe regimes (figures 8 and 9), the amplitude of the horizontal (vertical) velocity is largest in the high-shear (low-shear) regions.

Figure 10 presents the plot of maximal growth rates, in logarithmic coordinates, as a function of (Pe, Ri) for various density ratios (R_ρ). A reduction in R_ρ has a destabilizing effect on the system. The parameter space occupied by unstable modes tends to be very wide at low density ratios ($R_\rho = 1.5$ and $R_\rho = 2$ in figure 10a,b) and contracts with the increasing R_ρ ($R_\rho = 10$ and $R_\rho = 50$ in figure 10c,d). Likewise, the thermohaline–shear instability is sensitive to the diffusivity ratio (figure 11). For $\tau = 0.005$ (figure 11a) and $\tau = 0.1$ (figure 11b), unstable modes occupy most of the parameter space explored in figure 11. Increasing τ tends to stabilize the system. For $\tau = 1$, the dynamics of our system simplifies to that of an effectively one-component fluid, and the maximal unstable Richardson numbers reduce to the rather unremarkable interval of $Ri < 1$. While being of marginal relevance for our primary objective (i.e. explaining the origin of diffusive staircases), it is interesting to examine the case in figure 11(d). This configuration ($\tau = 1.5$) represents a fluid
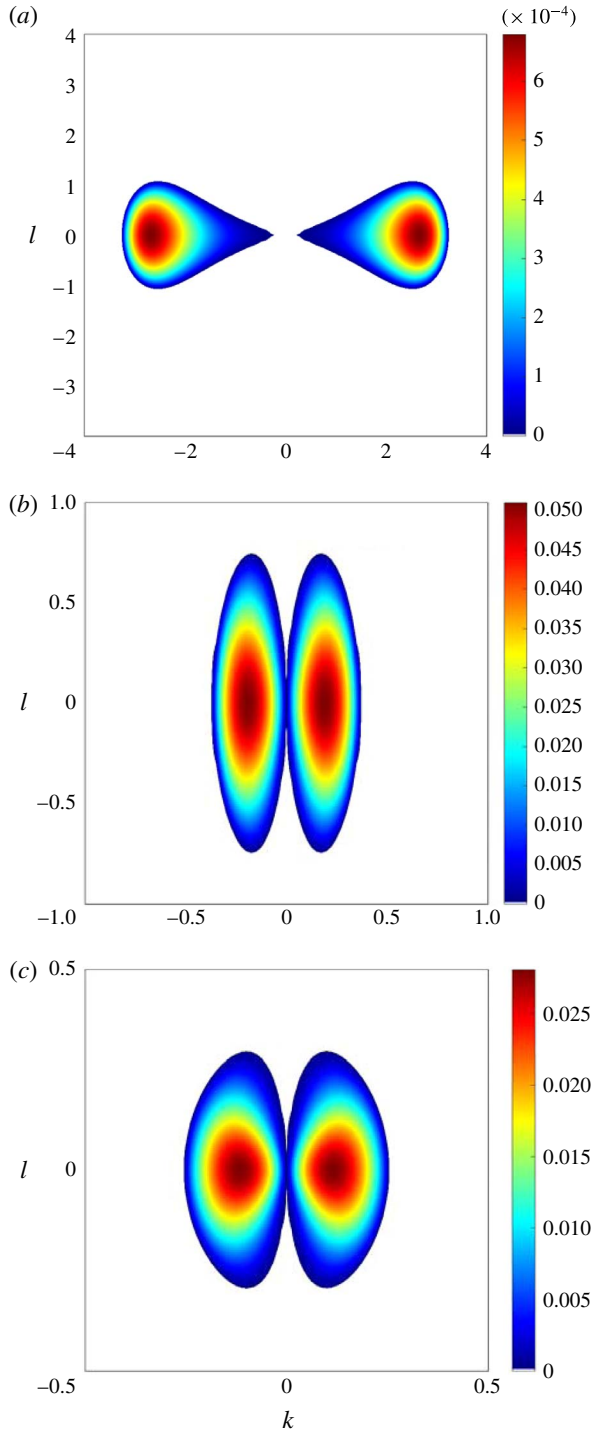
FIGURE 7. (Colour online) The growth rates $\mathrm{Re}(\lambda)$ predicted by the Floquet-based stability analysis are plotted as a function of the horizontal wavenumbers (k, l). Calculations are presented for $(Ri, Pe) = (1, 10^4), (1, 10^2), (10, 10^2)$ in $(a\text{--}c)$ respectively. Only positive growth rates are shown.
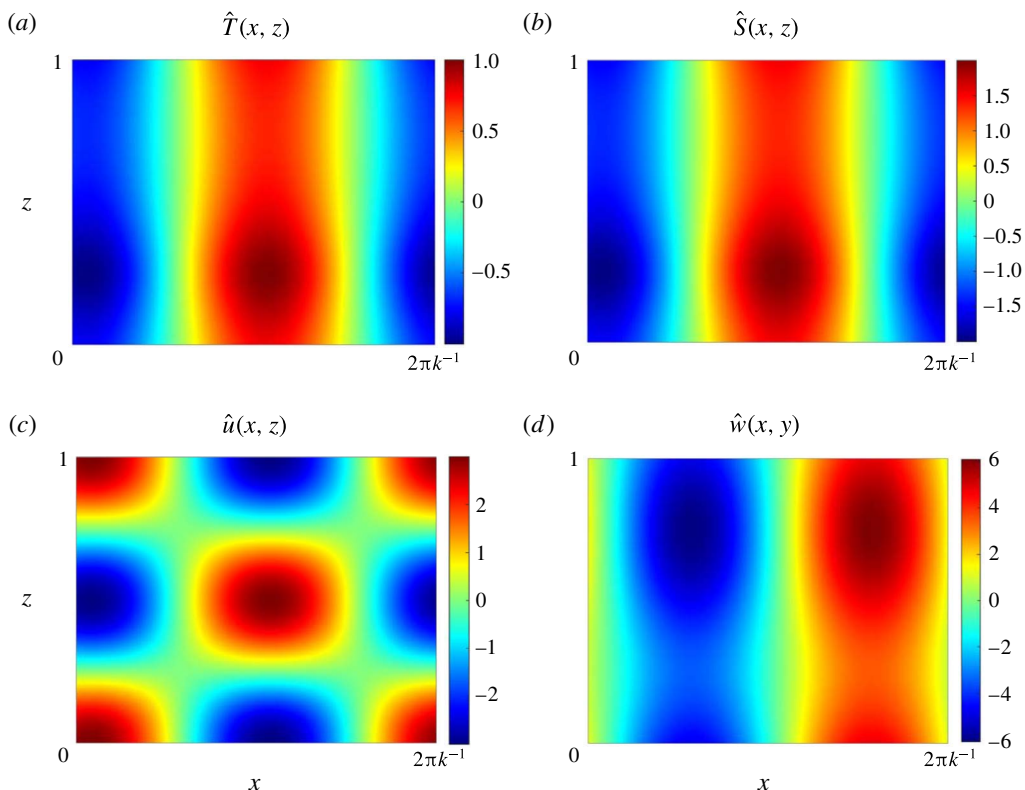
FIGURE 8. (Colour online) The most rapidly amplifying normal mode identified by a Floquet-based stability analysis for $(R_\rho, Ri, Pe, \tau) = (2, 1, 10^4, 0.01)$. The perturbation is normalized by the maximal temperature value. The patterns of T, S, u and w are shown in (*a–d*) respectively.

stratified in the fingering sense (the slower diffusing component is unstably stratified) but linearly stable with respect to double diffusion ($R_\rho > \tau$). Curiously, in this regime we find no evidence of new types of instability driven by a combination of shear and different molecular diffusivities of density components. Thus, thermohaline–shear destabilization appears to be an exclusively diffusive phenomenon.

5. Physical interpretation and energetics

In this section, an attempt is made to generate some insight into the dynamics of thermohaline–shear instability. One of the key questions in this regard is the ultimate source of energy required to amplify the unstable perturbations. The answer to this question is by no means obvious. The source of energy of Kelvin–Helmholtz instability is the kinetic energy of the basic shear, whereas double diffusion is driven by the release of potential energy stored in the unstably stratified density component. To identify the energy source for thermohaline–shear instabilities, the (non-dimensional) perturbation energy equation is derived as follows. First, we subtract the temperature and salinity equations in the linearized system (4.1), multiply the result by $(S - T)$, and integrate the result over one fundamental wavelength in x,
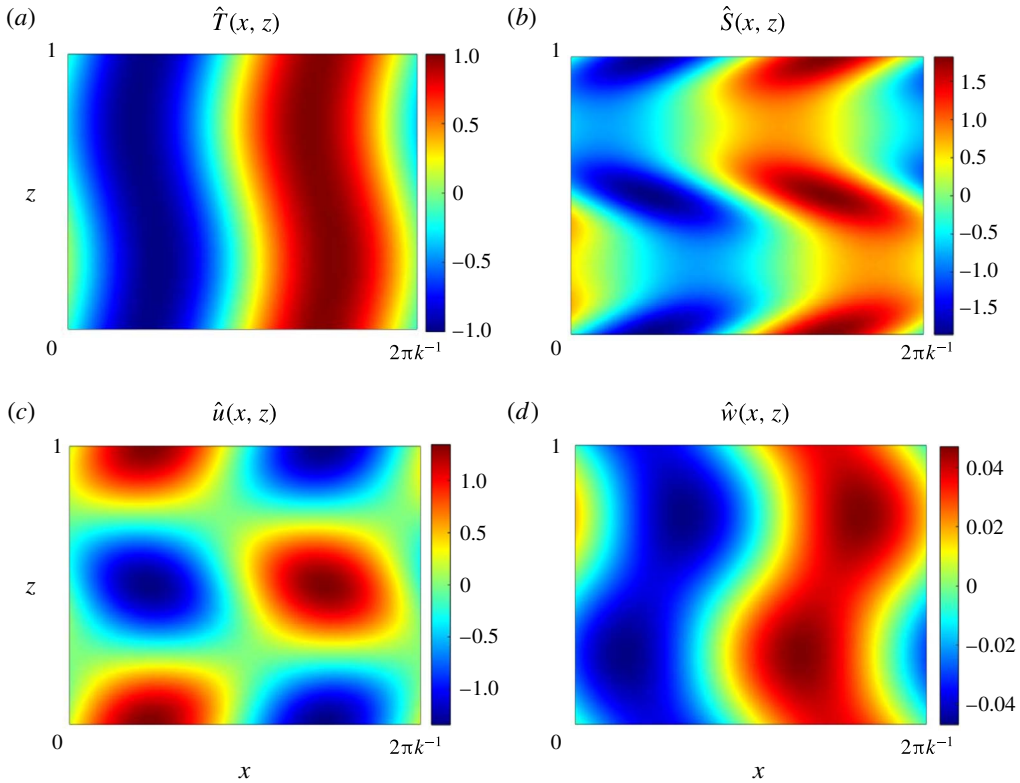
FIGURE 9. (Colour online) The same as figure 8 but for the low-Pe case $(R_\rho, Ri, Pe, \tau) = (2, 10, 10^2, 0.01)$.

y and z to obtain the density variance equation:

$$\frac{\partial}{\partial t} \int \frac{(S - T)^2}{2} \, \mathrm{d}V = \int (S - T)w(R_\rho - 1) \, \mathrm{d}V + \frac{1}{Pe} \int (S - T)\nabla^2(\tau S - T) \, \mathrm{d}V. \quad (5.1)$$

Similarly, the kinetic energy equation is obtained by multiplying the x, y and z momentum equations by u, v and w respectively, adding them, and integrating the result:

$$\frac{\partial}{\partial t} \int \frac{u^2 + v^2 + w^2}{2} \, \mathrm{d}V + \int \frac{\partial \bar{u}}{\partial z} uw \, \mathrm{d}V = \int \frac{4\pi^2 Ri}{R_\rho - 1}(T - S)w \, \mathrm{d}V$$
$$- \frac{Pr}{Pe} \int (|\nabla u|^2 + |\nabla v|^2 + |\nabla w|^2) \, \mathrm{d}V. \quad (5.2)$$

Next, the density variance equation (5.1) is multiplied by $(4\pi^2 Ri)/(R_\rho - 1)^2$ and added to the kinetic energy equation (5.2), which results in the total perturbation energy equation:

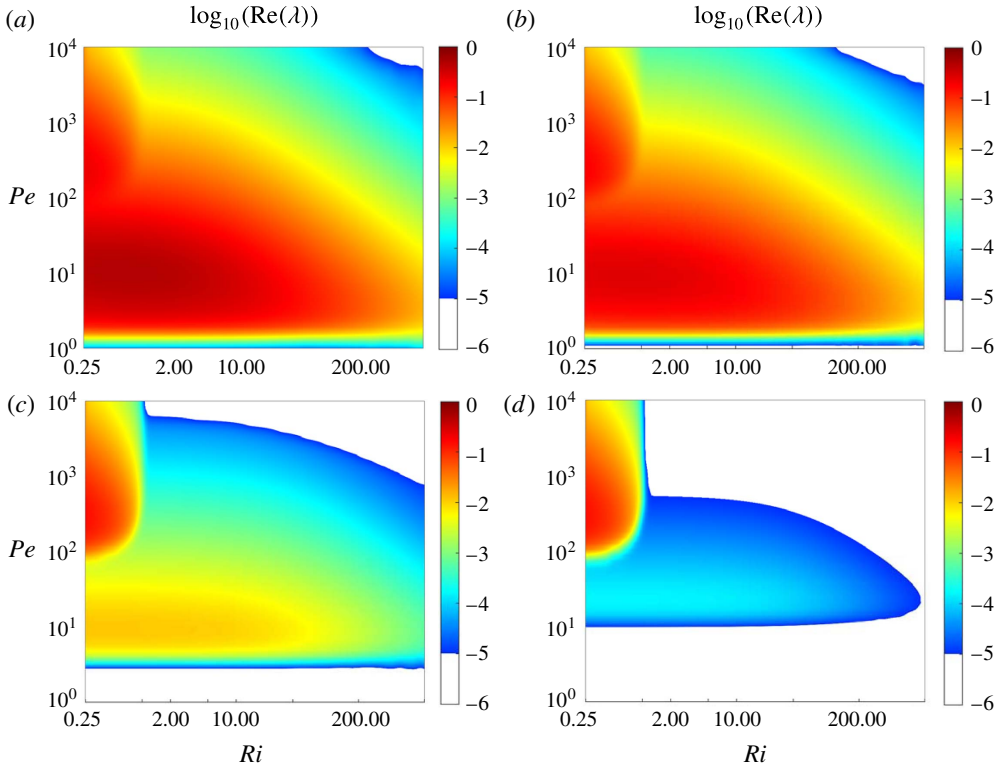$$\frac{\partial E}{\partial t} = P_{dd} + P_{sh} + P_{visc}, \quad (5.3)$$

FIGURE 10. (Colour online) The decimal logarithm of the maximal growth rate $\log_{10}(\text{Re}(\lambda))$ is plotted as a function of (Ri, Pe) for $R_\rho = 1.5, 2, 10$ and 50 in $(a\text{–}d)$ respectively for $\tau = 0.01$. Only the growth rates exceeding 10^{-5} are shown. One can note the reduction in the intensity of thermohaline–shear instability with increasing density ratio.

where

$$
\left.
\begin{aligned}
E &= \int \left(\frac{u^2 + v^2 + w^2}{2} + \frac{4\pi^2 Ri}{(R_\rho - 1)^2} \frac{(S - T)^2}{2} \right) \mathrm{d}V, \\
P_{dd} &= \frac{4\pi^2 Ri}{Pe(R_\rho - 1)^2} \int (S - T)\nabla^2(\tau S - T)\,\mathrm{d}V, \\
P_{sh} &= -\int \frac{\partial \bar{u}}{\partial z} uw\,\mathrm{d}V, \\
P_{visc} &= -\frac{Pr}{Pe} \int \left(|\nabla u|^2 + |\nabla v|^2 + |\nabla w|^2 \right) \mathrm{d}V.
\end{aligned}
\right\}
\tag{5.4}
$$

The P_{dd} term in (5.3) represents the production of perturbation energy by diffusion of heat and salt, P_{sh} is interpreted as the production of energy by shear, and P_{visc} is the viscous dissipation.

Finally, the individual terms in (5.3) were evaluated for the fastest growing normal modes identified using the linear analysis in §4. Of particular interest is the relative contribution of double-diffusive, shear-driven and viscous energy production/dissipation mechanisms. The answer turned out to be regime-dependent.
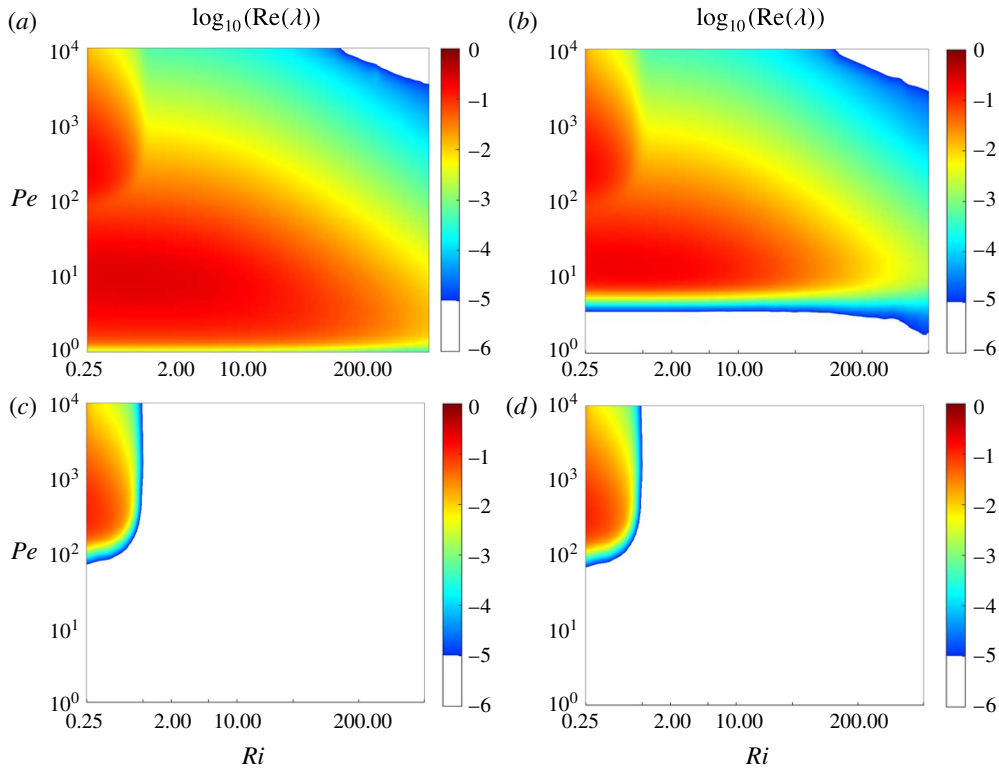
FIGURE 11. (Colour online) The decimal logarithm of the maximal growth rate $\log_{10}(\text{Re}(\lambda))$ is plotted as a function of (Ri, Pe) for $\tau = 0.005, 0.1, 1$ and 1.5 in $(a\text{–}d)$ respectively for $R_\rho = 2$. Only the growth rates exceeding 10^{-5} are shown. One can note the reduction in the intensity of thermohaline–shear instability with increasing diffusivity ratio.

Figure 12 shows the variation in the energy balance for a series of Floquet-based calculations in which Pe was systematically increased, whereas all other governing parameters were kept constant: $(R_\rho, Ri, \tau) = (2, 1, 0.01)$. The relative contribution of various processes is quantified by plotting

$$(P_{dd\,rel}, P_{sh\,rel}, P_{visc\,rel}) = \frac{(P_{dd}, P_{sh}, P_{visc})}{P_{dd} + P_{sh} + P_{visc}} \tag{5.5}$$

as a function of Pe. These diagnostics highlight the stark differences between the low-Pe and high-Pe regimes, which were evident in the DNS (§ 3) and in the linear stability analyses (§ 4). For high Peclet numbers ($Pe > 500$), the dominant balance is between the energy production by basic shear and its viscous dissipation. Nevertheless, double diffusion still accounts for a surprisingly large fraction of energy production ($P_{dd\,rel} = 0.55\text{–}0.65$). The reason for such a high double-diffusive contribution is that much of the perturbation kinetic energy produced by shear is immediately dissipated by viscosity.

The dynamics of low-Pe systems is dissimilar. The perturbation energy is produced almost entirely by double diffusion ($P_{dd\,rel} = 1.05\text{–}1.1$). The shear-driven contribution is small ($P_{sh\,rel} = 0.01\text{–}0.05$) and so is the viscous dissipation ($-P_{visc\,rel} = 0.05\text{–}0.15$).
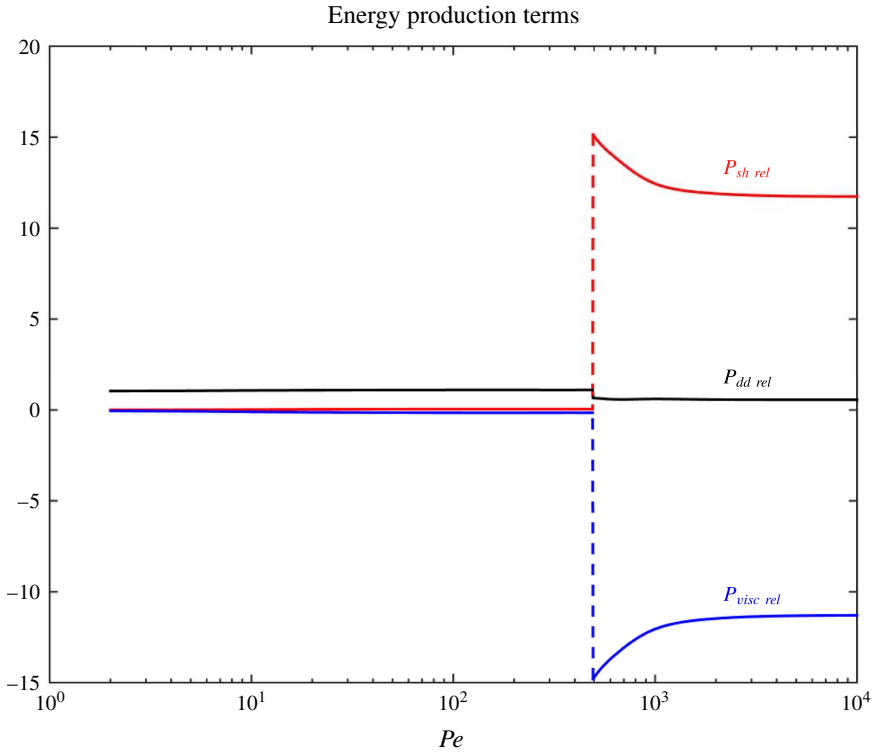
Energy production terms

FIGURE 12. (Colour online) The energy production/dissipation balances for various values of *Pe*. One can note the existence of two dynamically dissimilar regimes: (i) the high-*Pe* regime (*Pe* > 500) in which the dominant balance is between the production of the perturbation energy by shear and its viscous dissipation and (ii) the low-*Pe* regime (*Pe* < 500) in which the energy released by the unstable basic temperature gradient is transferred directly into the perturbation field, resulting in its amplification.

This result, however, should be interpreted with caution. Even though shear-induced effects are not strongly reflected in the energetics, it would be erroneous to conclude that they are largely irrelevant for the dynamics of thermohaline systems at low *Pe*. On the contrary, the release of potential energy by double diffusion is only possible due to the catalytic role of shear. In the absence of shear, the smooth thermohaline stratification in the oceanographically relevant parameter regime would be linearly stable.

The schematic diagram in figure 13 attempts to rationalize the destabilizing tendency of shear. Before delving into the dynamics of the interaction between shear and double diffusion, let us recall the conventional interpretation of oscillatory diffusive instability. A particle initially located at the equilibrium level (A) is slightly displaced (figure 13) upward into a colder and fresher region (A_1). In the absence of diffusion and friction, the particle would oscillate at the buoyancy frequency (N_b). However, since heat diffuses faster than salt, the particle quickly adjusts its temperature to its new environment, but largely retains its salinity. Thus, the particle is now denser than the surrounding fluid and the buoyancy force is downward. Therefore, as the particle moves downward, it gains extra kinetic energy due to the buoyancy forcing associated with the diffusion of heat. This energy gain on the way down is slightly higher than
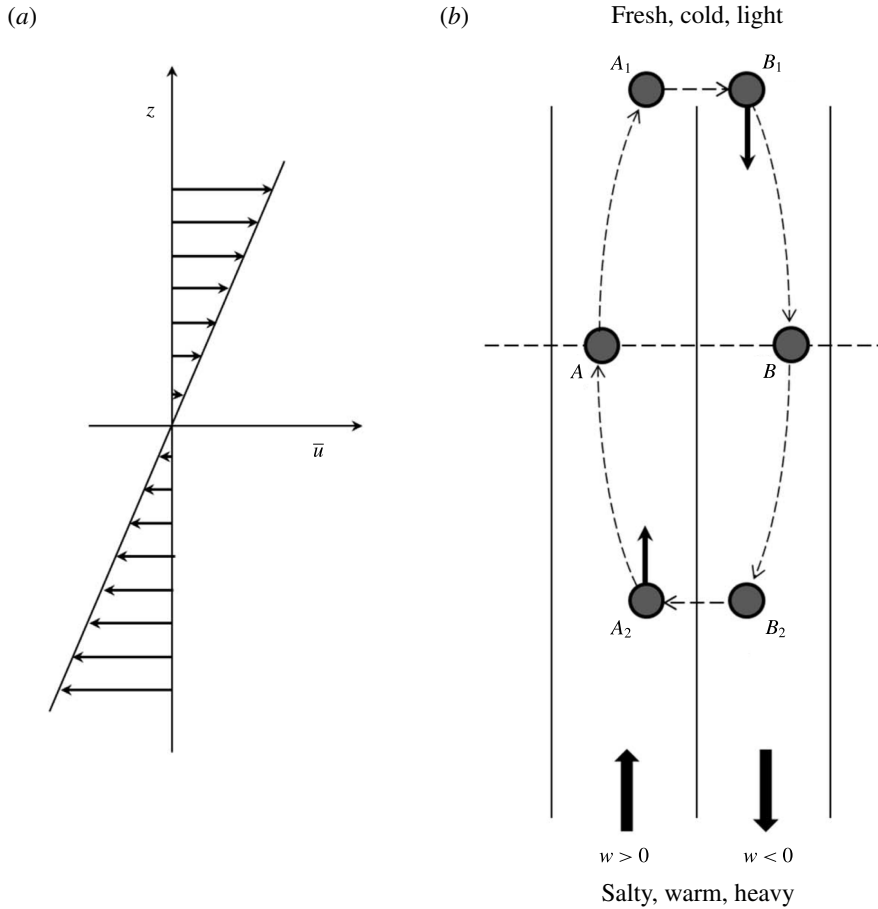
FIGURE 13. Schematic diagram illustrating the mechanism of thermohaline–shear instability. While diffusive instability is inherently oscillatory, and therefore highly susceptible to viscous damping, the presence of vertical shear allows for direct instability modes.

the corresponding loss of kinetic energy on the way up (the particle is colder on the downward part of the cycle) and therefore there is a small net gain of energy in each cycle. This residual gain can, in principle, drive amplifying (overstable) oscillations. However, the oscillatory nature of diffusive instability makes it highly vulnerable to friction, and therefore its parameter range (1.1) is extremely narrow.

Let us now consider the effects of vertical shear, as indicated in figure 13. In this configuration, possibilities exist not only for oscillatory but also for direct modes of instability. After the particle is displaced upward (from point A to A_1) and its buoyancy is reduced, it can be advected by the shear into the downward-moving region (B_1). As a result, the downward motion there is further reinforced by buoyancy forcing. Likewise, as the particle is displaced below the equilibrium level (B_2) and it becomes lighter than the surrounding fluid, it can be advected by shear into the upward-moving region (A_2). Thus, while individual Lagrangian particles in this configuration still inevitably oscillate, there is now a possibility for the direct amplification of the velocity field at any given point in space. This dynamics results in the direct – and

therefore much more efficient – transfer of energy from thermal stratification into amplifying perturbations. In the direct mode, the buoyancy forcing acts continuously to amplify the perturbation, rather than alternating between reinforcing and opposing action. The absence of fast oscillations in the Eulerian velocity field implies that the proposed mechanism is also less susceptible to viscous damping. Therefore, the parameter range for thermohaline–shear instability is much wider than for diffusive convection (figures 10 and 11), and the instability conditions are readily met in the ocean.

6. Discussion

Some of the most fascinating problems in instability theory arise when two independently stable processes lead to the destabilization of systems concurrently affected by both. A well-known example of this counterintuitive behaviour is the unstable system consisting of a vertically bounded uniform shear and bottom-heavy stratification, each of which is stable individually (Richardson 1920). Other cases that fall into the same category include the joint instability of rotating magnetic fields that are separately stable (Stern 1963) and the instability of a stable thermal stratification in the presence of a nominally stabilizing magnetic field (Hughes & Weiss 1995). Our study offers yet another example of such unexpected destabilization – dynamically and diffusively stable two-component shear flows. Linear stability analysis based on the Floquet theory demonstrates that shear flows can be unstable for surprisingly high values of the density ratio ($R_\rho \sim 10$) and Richardson number ($Ri \sim 10^3$). These values greatly exceed the individual thresholds for both dynamic and diffusive instabilities ($R_{\rho cr}, Ri_{cr}$) = (1.1, 0.25). Such a wide parameter range for thermohaline–shear instability includes typical parameters of the ocean regions characterized by thermohaline layering.

Thermohaline–shear instability exhibits many interesting and, in several ways, counterintuitive features. Depending on the parameter regime, the most rapidly amplifying unstable modes can be localized in low-shear or high-shear regions, and yet the presence of shear is absolutely essential. Thermohaline–shear instability rapidly intensifies with decreasing Ri, R_ρ and τ. As with Kelvin–Helmholtz instability, the most rapidly amplifying perturbations are aligned in the direction normal to the flow. The transition to fully three-dimensional patterns occurs only at the nonlinear evolutionary stages, characterized by the appearance of secondary instabilities. Multiple lines of evidence, stemming from DNS, Floquet stability analysis and arguments based on energetics, indicate the existence of two dynamically distinct regimes, realized for low and high Peclet numbers. The low-*Pe* regime is perhaps more interesting since its dissimilarities with one-component systems are most profound. In both low-*Pe* and high-*Pe* cases, most of the energy required for perturbation growth is supplied by the unstably stratified density component (T). In this regard, thermohaline–shear instability is similar to double diffusion, with shear flow playing a catalytic role in the amplification of perturbations. In the high-*Pe* case, however, a large amount of energy is supplied by the basic shear, but this gain is compensated by the equivalent energy loss due to viscous dissipation.

Finally, it should be emphasized that the effects discussed in this study should not be considered as merely an example of fluid-dynamical curiosity. Fully nonlinear simulations reveal that thermohaline–shear instability can reorganize smooth T–S fields into a series of mixed layers separated by thin high-gradient interfaces. These structures are suggestive of diffusive staircases, commonly observed in high-latitude

regions of the World Ocean (Arctic and Southern Oceans), which raises an intriguing question of whether the origin of staircases can be attributed to thermohaline–shear instability. In this regard, an important caveat of our analysis is the steady-state model of the background shear. The steady-state assumption made it possible to perform formal linear stability analysis in a straightforward manner and efficiently explore the parameter space. However, in the ocean, vertical fine-scale shear is largely associated with the internal wave field, and therefore it is neither steady nor unidirectional. It would be of interest to determine whether thermohaline–shear instability persists in stochastic wave-driven shears (e.g. Radko *et al.* 2015) and whether it produces layering as effectively as its steady-state counterpart. Other suggestions for future research include the development of laboratory-based analogues of the presented models. Free from computational constraints, experiments could be used to explore a wider parameter range and bring additional insights into the dynamics of thermohaline–shear instability.

Acknowledgements

REFERENCES

BALMFORTH, N. J. & YOUNG, Y.-N. 2002 Stratified Kolmogorov flow. *J. Fluid Mech.* **450**, 131–167.

BEBIEVA, Y. & TIMMERMANS, M.-L. 2016 An examination of double-diffusive processes in a mesoscale eddy in the Arctic Ocean. *J. Geophys. Res. Oceans* **121**, 457–475.

COLE, S. T., TIMMERMANS, M. L., TOOLE, J. M., KRISHFIELD, R. A. & THWAITES, F. T. 2014 Ekman veering, internal waves, and turbulence observed under Arctic sea ice. *J. Phys. Oceanogr.* **44**, 1306–1328.

FERNANDO, H. J. S. 1987 The formation of layered structure when a stable salinity gradient is heated from below. *J. Fluid Mech.* **182**, 525–541.

FLANAGAN, J., LEFLER, A. & RADKO, T. 2013 Heat transport through diffusive interfaces. *Geophys. Res. Lett.* **40**, 2466–2470.

HALLE, C. & PINKEL, R. 2003 Internal wave variability in the Beaufort Sea during the winter of 1993/1994. *J. Geophys. Res.* **108**, 3210.

HOLYER, J. Y. 1983 Double-diffusive interleaving due to horizontal gradients. *J. Fluid Mech.* **137**, 347–362.

HOWARD, L. N. 1961 Note on a paper of John W. Miles. *J. Fluid. Mech.* **10**, 509–512.

HUGHES, D. W. & WEISS, N. O. 1995 Double-diffusive convection with two stabilizing gradients: strange consequences of magnetic buoyancy. *J. Fluid Mech.* **301**, 383–406.

KELLEY, D. E., FERNANDO, H. J. S., GARGETT, A. E., TANNY, J. & OZSOY, E. 2003 The diffusive regime of double-diffusive convection. *Prog. Oceanogr.* **56**, 461–481.

LEVINE, M. D., PAULSON, C. A. & MORISON, J. H. 1985 Internal waves in the Arctic Ocean: comparison with lower-latitude observations. *J. Phys. Oceanogr.* **15**, 800–809.

MERRYFIELD, W. J. 2000 Origin of thermohaline staircases. *J. Phys. Oceanogr.* **30**, 1046–1068.

MILES, J. W. 1961 On the stability of heterogeneous shear flows. *J. Fluid. Mech.* **10**, 496–508.

RADKO, T. 2003 A mechanism for layer formation in a double-diffusive fluid. *J. Fluid Mech.* **497**, 365–380.

RADKO, T. 2007 Mechanics of merging event for a series of layers in a stratified turbulent fluid. *J. Fluid Mech.* **577**, 251–273.

RADKO, T. 2013 *Double-Diffusive Convection*. p. 344. Cambridge University Press.

RADKO, T. 2014 Applicability and failure of the flux-gradient laws in double-diffusive convection. *J. Fluid Mech.* **750**, 33–72.

RADKO, T., BALL, J., COLOSI, J. & FLANAGAN, J. 2015 Double-diffusive convection in a stochastic shear. *J. Phys. Oceanogr.* **45**, 3155–3167.

RADKO, T., BULTERS, A., FLANAGAN, J. & CAMPIN, J.-M. 2014a Double-diffusive recipes. Part 1: large-scale dynamics of thermohaline staircases. *J. Phys. Oceanogr.* **44**, 1269–1284.

RADKO, T., FLANAGAN, J., STELLMACH, S. & TIMMERMANS, M.-L. 2014b Double-diffusive recipes. Part 2: layer merging events. *J. Phys. Oceanogr.* **44**, 1285–1305.

RADKO, T. & STERN, M. E. 2011 Finescale instabilities of the double-diffusive shear flow. *J. Phys. Oceanogr.* **41**, 571–585.

RICHARDSON, L. F. 1920 The supply of energy from and to atmospheric eddies. *Proc. R. Soc. Lond.* A **97**, 354–373.

STELLMACH, S., TRAXLER, A., GARAUD, P., BRUMMELL, N. & RADKO, T. 2011 Dynamics of fingering convection II: the formation of thermohaline staircases. *J. Fluid Mech.* **677**, 554–571.

STERN, M. E. 1963 Joint instability of hydromagnetic fields which are separately stable. *Phys. Fluids* **6**, 636–642.

STERN, M. E. 2003 Initiation of a doubly diffusive convection in a stable halocline. *J. Mar. Res.* **61**, 211–233.

STERN, M. E., RADKO, T. & SIMEONOV, J. 2001 3D salt fingers in an unbounded thermocline with application to the Central Ocean. *J. Mar. Res.* **59**, 355–390.

THORPE, S. A., SMYTH, W. D. & LI, L. 2013 The effect of small viscosity and diffusivity on the marginal stability of stably stratified shear flows. *J. Fluid Mech.* **731**, 461–476.

TIMMERMANS, M.-L., TOOLE, J., KRISHFIELD, R. & WINSOR, P. 2008 Ice-tethered profiler observations of the double-diffusive staircase in the Canada Basin thermohaline. *J. Geophys. Res.* **113**, C00A02.

TURNER, J. S. 2010 The melting of ice in the Arctic Ocean: the influence of double-diffusive transport of heat from below. *J. Phys. Oceanogr.* **40**, 249–256.

TURNER, J. S. & STOMMEL, H. 1964 A new case of convection in the presence of combined vertical salinity and temperature gradients. *Proc. Natl Acad. Sci.* **52**, 49–53.

VERONIS, G. 1965 On finite amplitude instability in thermohaline convection. *J. Mar. Res.* **23**, 1–17.

WALIN, G. 1964 Note on stability of water stratified by both salt and heat. *Tellus* **18**, 389–393.